Published in Applied Physics Letters 88, issue 241118, 1-3, 2006
which should be used for any reference to this work

InP-based quantum cascade detectors in the mid-infrared

Marcel Graf,[a] Nicolas Hoyler, Marcella Giovannini, Jérôme Faist, and Daniel Hofstetter
Institute of Physics, University of Neuchâtel, Rue A.-L. Breguet 1, 2000 Neuchâtel, Switzerland

We present two InP-based quantum cascade detectors (QCDs) in the mid-infrared wavelength range. Their narrow band detection spectra are centered at 5.3 and 9 μm. A vertical intersubband transition followed by a carefully designed extraction cascade, which is adapted to the LO-phonon energy, leads to 10 K responsivities $\mathcal{R}$ of 3.2 and 9.0 mA/W and background limited detectivities $\mathcal{D}^*_{\mathrm{BLIP}}$ of 2×10^8 and 3×10^9 Jones, for the 5.3 and the 9 μm devices, respectively. Detection has been observed up to device temperatures of 300 K (RT), albeit reasonable performance is restricted to temperatures below 150 K (5.3 μm) and 70 K (9 μm). Designed for zero bias operation, QCDs do not produce any dark current and therefore do not suffer from dark current noise and capacitance saturation at long integration times, making them ideal devices for large focal plane arrays.

Semiconductor-based mid-infrared detectors have a wide range of potential applications in sensing, security, and defense. The probably most advanced technology using these materials is the quantum well infrared photodetector (QWIP).[1,2] This device utilizes bound-to-continuum intersubband transitions in quantum wells, generally operates in a photoconductive mode, and is typically held at cryogenic temperatures. Photovoltaic QWIPs (PV-QWIPs), having a built-in asymmetry which allows biasless operation,[3] have been shown to work up to room temperature.[4] Other promising solutions include interband mercury-cadmium-telluride detectors[5] and silicon microbolometers.[6] The former devices are quite rapid when used at 300 K, but are not very good in terms of signal-to-noise ratio. By cooling to 77 K, one can gain several orders of magnitude of signal-to-noise ratio, but the detectors then become slow. Microbolometers, finally, have made astonishing progress in the last couple of years and are now used in infrared camera systems. Recently, quantum cascade structures have been used for the detection of infrared radiation.[7–9] Compared to photoconductive QWIPs, this concept shares the advantage of a photovoltaic detection scheme with PV-QWIPs: as no bias voltage is applied, no dark current noise and no integration-time limitation due to capacitance saturation in the readout circuit occur. By using InP-based instead of GaAs-based materials, one can gain nearly a factor of 2 in absorption efficiency because of the lighter effective mass. Furthermore, the wells can be grown somewhat wider leading to less linewidth broadening due to interfacial roughness.[10] Additional performance improvements are expected because of the bound-to-bound transition, which leads to narrower detection peaks and thus a better noise figure.[11] Keeping in mind the fabrication technology, it is finally clear that in a QWIP, both conduction band discontinuity *and* well width are crucial parameters for high performance. In a QCD, these two parameters are not directly coupled, so that growth uncertainties in composition or thickness, leading to shifted energies of the states, will only slightly shift the detection wavelength, whereas the resulting misalignment of the upper state and the continuum in a QWIP significantly changes the escape probability which might severely degrade performance. In our presented structures, we refined the concept of the QCD, especially in terms of electron extraction. The energy levels of the "transport ramp" are now carefully designed to be in LO-phonon resonance for each transition between two consecutive levels.

Our QCDs are based on a vertical transition between two bound states in a Si-doped quantum well, whose excited state is coupled to the uppermost state of a chirped superlattice. This superlattice forms some kind of a "quantum stair" and allows extraction of the electrons from the upper state to the ground state of the following period. In this work, we investigated two different devices: sample N538 for a detection wavelength of 5.3 μm and sample N516 for 9.0 μm. The layer sequence of the two structures is shown in Table I.

In Fig. 1, a conduction band diagram of sample N538 is presented. The quantum stair formed by LO-phonon energy steps is clearly visible. By absorbing incident photons, electrons are excited from the ground state to states 8 and 9, with respective transition energies of 230 and 237 meV. From these coupled states ($\Delta E = 5-10$ meV) they either jump back (not contributing to detection) or, by emission of a LO phonon, jump down to state 7. Once there, a series of transitions down to the ground state of the adjacent period takes place. Since all subsequent transition energies are 34 meV, the resulting lateral displacement of the electrons should be very fast. The design for 9 μm detection wavelength is similar; a reduced number of steps in the extraction cascade complies with the lower energies (126 and 130 meV) of the vertical optical transitions.

These structures were grown on semi-insulating InP substrates by means of molecular beam epitaxy. On top of a 6000 Å thick n-doped (1.6×10^{18} cm^{-3} for N538 and 1.0×10^{18} cm^{-3} for N516) InGaAs contact layer, N detector periods as listed in Table I were grown. On top of this active region, we put a single 20 Å InAlAs barrier and a 2000 Å thick InGaAs layer with identical doping as the corresponding bottom contact. For better Ohmic behavior, this structure was overgrown with an alloyed contact consisting of an InAs–InGaAs superlattice with continuously rising doping density. The overall composition and the period of the active region superlattice were confirmed by x-ray diffraction. The

[a]Electronic mail: marcel.graf@unine.ch

TABLE I. Layer sequences for the samples N516 (9 μm) and N538 (5.3 μm). b denotes InAlAs barrier thickness in Å, w InGaAs well thickness in Å, and values in bold indicate the Si-doped layer, producing an effective sheet carrier density n_s.

	E_{trans} (eV)	N	w	b	w	b	w	b	w	b	w	b	w	b	w	b	w	b	n_s (cm^{-2})
N516	0.13	50	**100**	47	39	25	43	19	54	16	66	17							5×10^{11}
N538	0.23	30	**59**	60	17	44	20	39	23	37	27	35	32	31	39	28	47	26	2.36×10^{11}

measured superlattice period deviated from design by roughly 3% for N538 and by less than 0.3% for N516. After growth, the samples were processed into square shaped mesas of three different sizes (300, 200, and 100 μm) using standard photolithography and wet etching with aged $HBr:HNO_3:H_2O$ etch (1:1:10). On the top of the mesas as well as in the etched areas, we deposited Ohmic metallization layers (Ti, Au, Ge, Ag, Au/1.5, 12, 27, 50, 350 nm) which were annealed at 360 °C for 60 s. For efficient light coupling during optical characterization, the cleaved samples were polished into one sided 45° wedges. All measurements were done with the sample soldered on a copper submount held on the cold finger of a flow cryostat, and cooled using either liquid helium or liquid nitrogen.

For both samples and two different device sizes per sample, series of I-V curves at different device temperatures have been measured under dark conditions. For this experiment, the devices were optically and thermally shielded by an aluminum foil wrapped around the cryoshield of the cryostat. The dark I-V curves for one 9 μm device size are shown in Fig. 2. The kinks seen for both positive and negative voltages are due to special alignment configurations in the band structure: Since each period contains a quantum stair, one can find external fields for which the ground state of one period's stair is in resonance with the first or a higher excited state of the next period's stair. Under these conditions, transport is particularly efficient, leading to an increased conductivity. This is the case for −4, −2.5, and −1.4 V as well as for +3 V.

Activation energies for both samples were obtained from Arrhenius plots of the current at 50 mV applied bias. The activation energies obtained are 76 and 149 meV for the 9 and the 5.3 μm devices, which is only about 60% of the optical transition energy, corresponding to the transition from the ground state to state 5 in the 27 Å well. This leads to lower resistances and more Johnson noise at elevated device temperatures. As this reduces performance, this will be corrected by employing a slightly thicker extraction barrier in future experiments.

Optical characterization was performed in a Bruker Fourier-transform infrared spectrometer (FTIR) using the internal glowbar as light source. Absorption spectra were obtained by measuring the transmission through a multipass waveguide in double 45° facet configuration and for TE- and TM-polarized light. Photocurrent measurements were obtained by feeding the amplified signal produced by the device to the FTIR's external detector port. Based on these photocurrent spectra and the known intensity of the incident radiation, we calculated the responsivity spectra, shown in Fig. 3 together with the corresponding absorption spectra. One clearly sees the good match between the narrow band detection current, the absorption peaks, and the designed wavelengths for both devices. The detector at 5.3 μm works with a linewidth of 10 meV. Given the central transition energy of 235 meV, we thus observe a relative linewidth of 4.3%. The 9 μm device has roughly the same full width at half maximum (FWHM), but since the transition is smaller (140 meV), the relative linewidth is 7.1% in this case. It is obvious that in both samples, the responsivity peaks at a slightly higher energy than the absorption. This can be explained by the absorption taking place at the lowest possible energy, whereas transport is favored by the lowest possible remaining barrier height. In addition, the absorption is somewhat broader than the photocurrent signal. Here again, absorption into two separate levels is possible, whereas transport will be mainly from the upper level of the duplet.

In the upper part of Fig. 4, we show the peak responsivity as function of temperature for both devices. The lower part of Fig. 4 is a comparison of several limiting detectivities $\mathcal{D}^*$, with the observered noise behavior as function of temperature. First, there is the Johnson noise limited $\mathcal{D}^*_J$ for both detectors, based on the temperature dependent device resistance. Second, the background limited detectivity $\mathcal{D}^*_{\text{BLIP}}$ due to the photon noise of the background blackbody (at 300 K)

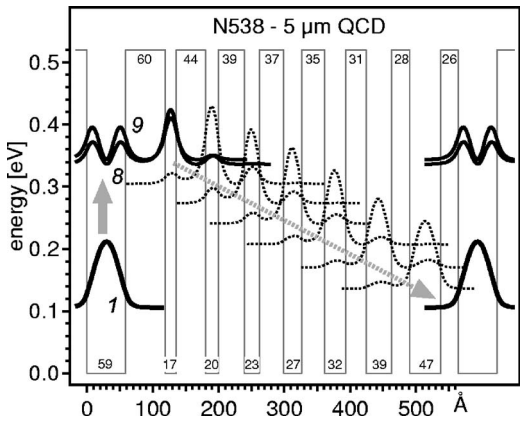

FIG. 1. Schematic conduction band structure of the 5.3 μm detector. Shown are the squared moduli of the relevant wave functions. The grey arrows show the transport of the electrons through the structure.

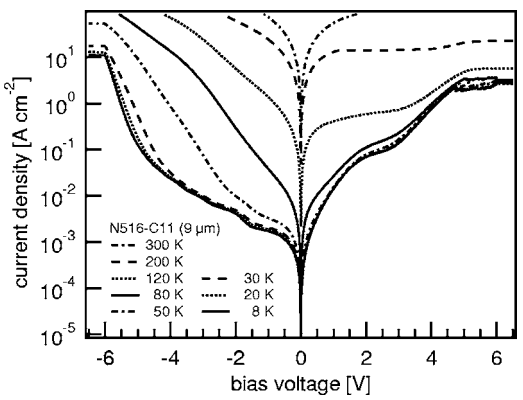

FIG. 2. Series of I-V curves for N516 (9 μm) between 8 and 300 K. The kinks correspond to special alignment conditions between states of the extraction quantum stair and the ground state.

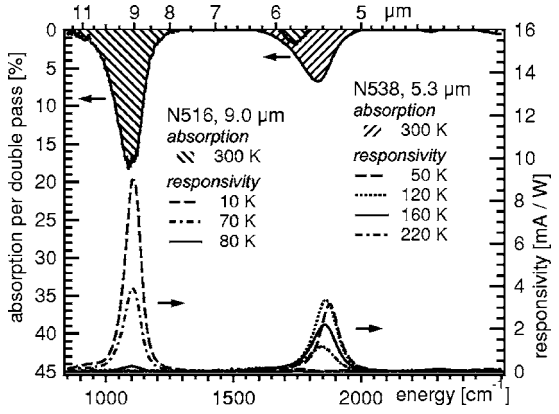

FIG. 3. Absorption at room temperature ("hanging" from the top axis) and responsivity measurements at different device temperatures and for both structures.

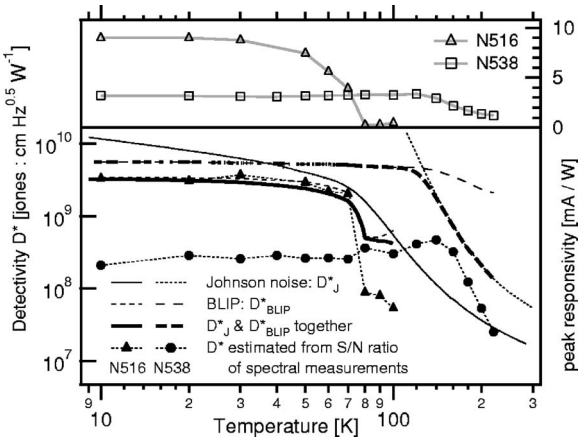

FIG. 4. Responsivity and detectivity as functions of temperature for both devices.

irradiation, seen with an opening solid angle of 2π, is plotted. The temperature where the two curves intersect defines T_{BLIP} for each detector, namely, 70 K for the 9 μm device and 150 K for the 5.3 μm device. The bold curves show the combined $\mathcal{D}^*$ from these two noise sources, and finally, the dots and triangles show directly measured detectivities, based on signal-to-noise ratios of the measured interferograms, the overall electrical bandwidth of the amplification chain including analog-to-digital conversion (ADC), the detectors' surfaces, and the known incident power of the illumination.

Based on the size of the observed photocurrents and the intensity of the incoming radiation, we determined also the responsivity of these QCDs. Peak responsivities in the background limited infrared photodetector (BLIP) regime are $\mathcal{R}$=9.0 mA/W for the 9 μm detector and $\mathcal{R}$=3.2 mA/W in the case of the 5.3 μm device. These values need to be compared with the theoretical maxima of $\mathcal{R}_{\mathrm{max}}=p_{\mathrm{abs}}\cdot e/h\nu\cdot 1/N\cdot p_e/p_c$. Given a capture probability of $p_c=1$ and a yet unknown escape probability p_e, the comparison of this theoretical limit with the experiment results in escape probabilities p_e of 0.33 and 0.34, respectively, for both devices, which coincide well with the following rough estimation: Since the upper state is a duplet, there is only about a 50% chance for the excited electrons to escape from the main well and to contribute to the current transport.

The most prominent observation of Figs. 3 and 4 is certainly that the responsivity, which is supposed to be temperature independent, drops significantly above T_{BLIP}. This behavior has several possible reasons: First, thermal backfilling of the first step level (only 32 meV above the ground state) results in a smaller absorption from the ground state; second, the escape probability is reduced due to a phonon scattering induced shortening of the upper state relaxation time; and third, the smaller device resistance at elevated temperatures severely hampers unidirectional transport of electrons. We believe that the third reason is likely the dominant one in our structures.

Careful optimization of the barrier thicknesses and the dopant concentration together with an enhanced optical coupling (diffraction grating) will raise the absorption probability, p_{abs}, and allow us to reduce the number of periods, leading to significant overall performance improvements, as the responsivity $\mathcal{R}_{\mathrm{max}}$ is proportional to $p_{\mathrm{abs}}\cdot 1/N$.

In summary, we demonstrated InP-based QCDs at 5.3 and 9 μm. We operated these detectors between 10 and 160 K. Maximal reponsivities $\mathcal{R}$ of 9.0 (9 μm) and 3.2 mA/W (5.3 μm) and detectivities of $\mathcal{D}^*_{\mathrm{BLIP}}=3\times10^9$ Jones at T_{BLIP}=70 K for the 9 μm device and 2×10^8 Jones at 150 K for the 5.3 μm detector have been achieved.

The authors acknowledge financial support from the Professorship Program of the Swiss National Science Foundation.

[1] H. C. Liu, R. Dudek, A. Shen, E. Dupont, C. Y. Song, Z. R. Wasilewski, and M. Buchanan, Appl. Phys. Lett. **79**, 4237 (2001).
[2] B. F. Levine, K. K. Choi, C. G. Bethea, J. Walker, and R. J. Malik, Appl. Phys. Lett. **50**, 1092 (1987).
[3] C. Schönbein, H. Schneider, G. Bihlmann, K. Schwarz, and P. Koidl, Appl. Phys. Lett. **68**, 973 (1996).
[4] H. Schneider, C. Schönbein, G. Bihlmann, P. van Son, and H. Sigg, Appl. Phys. Lett. **70**, 1602 (1997).
[5] L. T. Specht, W. E. Hoke, S. Oguz, P. J. Lemonias, V. G. Kreismanis, and R. Korenstein, Appl. Phys. Lett. **48**, 417 (1986).
[6] D. Murphy, M. Ray, R. Wyles, J. Asbrock, N. Lum, J. Wyles, C. Hewitt, A. Kennedy, and D. V. Lue, Proc. SPIE **4820**, 208 (2002).
[7] L. Gendron, C. Koeniguer, V. Berger, and X. Marcadet, Appl. Phys. Lett. **86**, 121116 (2005).
[8] D. Hofstetter, M. Beck, and J. Faist, Appl. Phys. Lett. **81**, 2683 (2002).
[9] M. Graf, G. Scalari, D. Hofstetter, J. Faist, H. Beere, E. Linfield, D. Ritchie, and G. Davies, Appl. Phys. Lett. **84**, 475 (2004).
[10] C. Pflugl, W. Schrenk, S. Anders, G. Strasser, C. Becker, C. Sirtori, Y. Bonetti, and A. Muller, Appl. Phys. Lett. **83**, 4698 (2003).
[11] K. M. S. V. Bandara, J.-W. Choe, M. H. Francombe, A. G. U. Perera, and Y. F. Lin, Appl. Phys. Lett. **60**, 3022 (1992).